Phase separation in the outer membrane of *Escherichia coli*

Georgina Benn[a,b,c], Irina V. Mikheyeva[d], Patrick George Inns[e], Joel C. Forster[f,g,h], Nikola Ojkic[f], Christian Bortolini[a], Maxim G. Ryadnov[c,i], Colin Kleanthous[e,1], Thomas J. Silhavy[d,1], and Bart W. Hoogenboom[a,b,f,g,1]

[a]London Centre for Nanotechnology, University College London, London WC1H 0AH, United Kingdom; [b]Institute of Structural and Molecular Biology, University College London, London WC1E 6BT, United Kingdom; [c]National Physical Laboratory, Teddington TW11 0LW, United Kingdom; [d]Department of Molecular Biology, Princeton University, Princeton, NJ 08544; [e]Department of Biochemistry, University of Oxford, Oxford OX1 3QU, United Kingdom; [f]Department of Physics and Astronomy, University College London WC1E 6BT London, United Kingdom; [g]Institute for the Physics of Living Systems, University College London WC1E 6BT London, United Kingdom; [h]Medical Research Council Laboratory for Molecular Cell Biology, University College London, London WC1E 6BT, United Kingdom; and [i]Department of Physics, King's College London, London WC2R 2LS, United Kingdom

Edited by Joe Lutkenhaus, University of Kansas Medical Center, Kansas City, KS, and approved September 20, 2021 (received for review July 2, 2021)

Gram-negative bacteria are surrounded by a protective outer membrane (OM) with phospholipids in its inner leaflet and lipopolysaccharides (LPS) in its outer leaflet. The OM is also populated with many β-barrel outer-membrane proteins (OMPs), some of which have been shown to cluster into supramolecular assemblies. However, it remains unknown how abundant OMPs are organized across the entire bacterial surface and how this relates to the lipids in the membrane. Here, we reveal how the OM is organized from molecular to cellular length scales, using atomic force microscopy to visualize the OM of live bacteria, including engineered *Escherichia coli* strains and complemented by specific labeling of abundant OMPs. We find that a predominant OMP in the *E. coli* OM, the porin OmpF, forms a near-static network across the surface, which is interspersed with barren patches of LPS that grow and merge with other patches during cell elongation. Embedded within the porin network is OmpA, which forms noncovalent interactions to the underlying cell wall. When the OM is destabilized by mislocalization of phospholipids to the outer leaflet, a new phase appears, correlating with bacterial sensitivity to harsh environments. We conclude that the OM is a mosaic of phase-separated LPS-rich and OMP-rich regions, the maintenance of which is essential to the integrity of the membrane and hence to the lifestyle of a gram-negative bacterium.

gram-negative bacteria | outer membrane | phase separation | atomic force microscopy

Diderm bacteria, such as *Escherichia coli*, are surrounded by an outer membrane (OM) that protects cells against the immune systems of plants and animals, contributes to the mechanical stability of the cell, and excludes many classes of antibiotics, thereby contributing to antimicrobial resistance (1, 2). The OM is comprised of an asymmetric bilayer of phospholipids in the inner leaflet, lipopolysaccharides (LPS) in the outer leaflet, and many outer-membrane proteins (OMPs). OMPs are hugely diverse β-barrel proteins that can be present at hundreds to hundreds of thousands of copies per cell (3). They have been shown to be relatively static (4), probably due to promiscuous protein–protein interactions and binding of LPS that exists in a slow-moving, liquid-crystalline state (5, 6). Using fluorescent labels, some OMPs have been shown to cluster into supramolecular islands of ∼0.3- to 0.5-μm sizes (4, 7–9). However, it remains unknown how abundant OMPs are organized across the entire bacterial surface and how this relates to the lipids in the membrane.

To address this fundamental question, we have imaged the entire surface of live and metabolically active bacteria at nanometer resolution using atomic force microscopy (AFM). Applying such large-scale, high-resolution imaging on engineered *E. coli* strains and complementing it by specific labeling of abundant OMPs, we identify large-scale and near-static protein-rich networks interspersed with nanoscale domains that are enriched in LPS. Key components of the protein-rich networks are abundant trimeric porins such as OmpF, in addition to (the monomeric) OmpA, which forms noncovalent interactions to the underlying cell wall (10). By contrast, no significant protein content is detected in the LPS-rich domains, which are also found to grow and merge with other patches during cell elongation. When the LPS–phospholipid asymmetry of the OM is perturbed by mislocalization of phospholipids to the outer leaflet (11), we find deformation of the membrane rather than expansion of LPS patches, indicating the appearance of a new, phospholipid-enriched phase at the bacterial surface.

Results

Identification of Networks of Trimeric Porins Spanning the Bacterial Surface. To resolve the supramolecular organization of the unlabeled OM in live bacteria, *E. coli* were immobilized onto glass coverslips and imaged by AFM in minimal media (12, 13). AFM images labeled "phase" represent the variation in the phase of the oscillating AFM probe, which depends on

Significance

Antimicrobial resistance is particularly prevalent in gram-negative bacteria, as antibiotics that act inside the cells must overcome their outer membrane. So far, technical limitations have prevented us from determining how outer-membrane proteins and lipids are organized to form this functional barrier. Here, we use nanoscale imaging of live bacteria to reveal that the most abundant outer-membrane proteins form a network that spans the entire bacterial surface, leaving only small gaps of phase-separated lipopolysaccharide. This tendency to phase separate is further emphasized by the formation of new domains when phospholipids are mislocated at the surface, rendering cells more susceptible to some antibiotics. Overall, the phase-separated nature of the outer membrane defines a perspective on its integrity and barrier function.

Author contributions: G.B., M.G.R., C.K., T.J.S., and B.W.H. designed research; G.B., I.V.M., P.G.I., J.C.F., N.O., and C.B. performed research; G.B., I.V.M., P.G.I., J.C.F., N.O., C.B., C.K., T.J.S., and B.W.H. analyzed data; and G.B., I.V.M., P.G.I., J.C.F., N.O., C.B., M.G.R., C.K., T.J.S., and B.W.H. wrote the paper.

The authors declare no competing interest.

This article is a PNAS Direct Submission.

[1]To whom correspondence may be addressed. Email: colin.kleanthous@bioch.ox.ac.uk, tsilhavy@princeton.edu, or b.hoogenboom@ucl.ac.uk.

This article contains supporting information online at http://www.pnas.org/lookup/suppl/doi:10.1073/pnas.2112237118/-/DCSupplemental.

Published October 29, 2021.

local material properties (14). In contrast to the simultaneously acquired surface topography (height), the phase allowed us to view molecular-scale detail against a background that was less affected by variations of the surface topography seen at cellular length scales. At a low magnification, cells had a smooth appearance (Fig. 1*A*). By recording multiple higher-magnification scans and overlaying these to obtain a cell-wide, molecular-scale map of the accessible OM, the bacterial surface was shown to contain a dense packing of pores, superposed to a background with 2- to 5-nm height variations at a ∼50-nm length scale (Fig. 1 *B* and *C* and *SI Appendix*, Fig. S1*A*).

To aid the assignment of the observed pore structures, each pore was localized and the pore packing quantified via the nearest-neighbor distance (∼9 nm) and angular distribution of near neighbors (peaked just below 60°; *SI Appendix*, Fig. S1 *B* and *C*). This is locally consistent with the hexagonal lattices of porin trimers reconstituted in lipid membranes (15–20), with one observable pore for each trimer. The ∼8-nm diameter of observed pores also fits well with the dimensions from crystal structures of trimeric porins (21). We therefore attributed the pore network to trimeric porins. This interpretation was confirmed by modulation of the expression of the most abundant trimeric porins, OmpF and OmpC, via the removal and reintroduction of their transcriptional activator, OmpR (22) (Fig. 1*D*). This removal greatly reduced the number of pores per unit area (square micrometers), and its reintroduction led to increasing amounts of pores (Fig. 1 *E* and *F*), showing similar trends as the *ompF* and *ompC* expression (Fig. 1*D*). Similar results were also obtained on a different *E. coli* strain without trimeric porins OmpF, OmpC, and LamB, in which cells had no pore features in AFM images (*SI Appendix*, Fig. S1*A*), confirming that the observed pores correspond to trimers of porins. This was independent of LPS levels, as these were not affected by the removal of trimeric porins (*SI Appendix*, Fig. S1 *D* and *E*).

The pores in these cell-wide networks showed very low mobility: by AFM, we found a low median diffusion coefficient of 2×10^{-7} $\mu m^2 \cdot s^{-1}$. By single-molecule fluorescence microscopy, the median diffusion coefficient of OmpF was measured (at lower spatial resolution) as 0.0018 $\mu m^2 \cdot s^{-1}$ for live cells, not significantly higher than control experiments on fixed cells (*SI Appendix*, Fig. S2). The crowded and static nature of this trimeric porin network is remarkable, as the OM expands and rearranges at cellular length scales during growth.

LPS Patches Provide Openings in the Proteinaceous Network. Presuming that membrane biogenesis implies a substantial supramolecular rearrangement and the ready formation of defects, the dense porin network was inspected for interruptions. By imaging the whole cell, sparse, pore-free, smooth patches were revealed, protruding by ∼0.5 to 1 nm above the pore network (Fig. 2 *A* and *B*). The patches are ∼25 to 225 nm wide, with a mean diameter of 55 nm, and were found on all cells. We note the similarity of these observations to early freeze-fracture electron microscopy images (23–26), yet here, we consistently observed such patches on live and dividing bacteria (*SI Appendix*, Fig. S3 *A* and *B*). Strikingly, patches appeared to behave as liquid phases in the membrane: merging, growing, and splitting apart over long time periods but maintaining their approximate

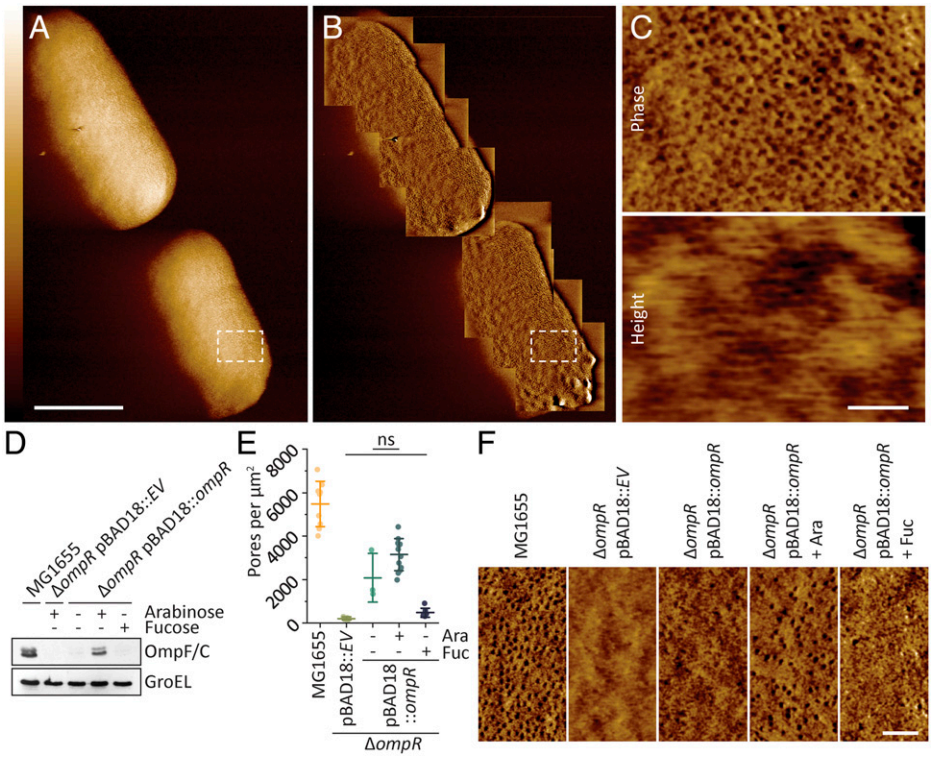

Fig. 1. The OM contains a dense, crowded network of trimeric porins. (*A*) Large AFM phase scans show a MG1655 cell at low resolution, and (*B*) images of the nanoscale architecture of the entire OM can be produced by superimposing small, high-resolution phase images. (*C*) Enlarged phase and height images of the region marked by the dashed box in *A* and *B* show the OM covered by a network of ∼8-nm-wide pores. (*D*) Western blot showing variation in the levels of expression of OmpF and OmpC by the removal of *ompR* and its reintroduction on an inducible plasmid. (*E*) Number of pores per square micrometer detected in AFM images, showing that removal of *ompR* leads to the disappearance of the pores. Subsequent reintroduction of *ompR* leads to an increase in pores with OmpF and OmpC expression. Each data point corresponds to one cell with at least three independent experiments for each condition. (*F*) Typical phase images used for the quantification in *E*. [Scale bars: (*A*) 500 nm and (*C* and *F*) 50 nm.] Color phase (measured in degrees [deg]) and height scales are (*A*) 7 deg, (*B*) 1.5 deg, (*C*) 1.5 deg and 5 nm, and (*F*) 2 deg, 2 deg, 1 deg, 2 deg, and 1 deg. ns = $P > 0.5$.

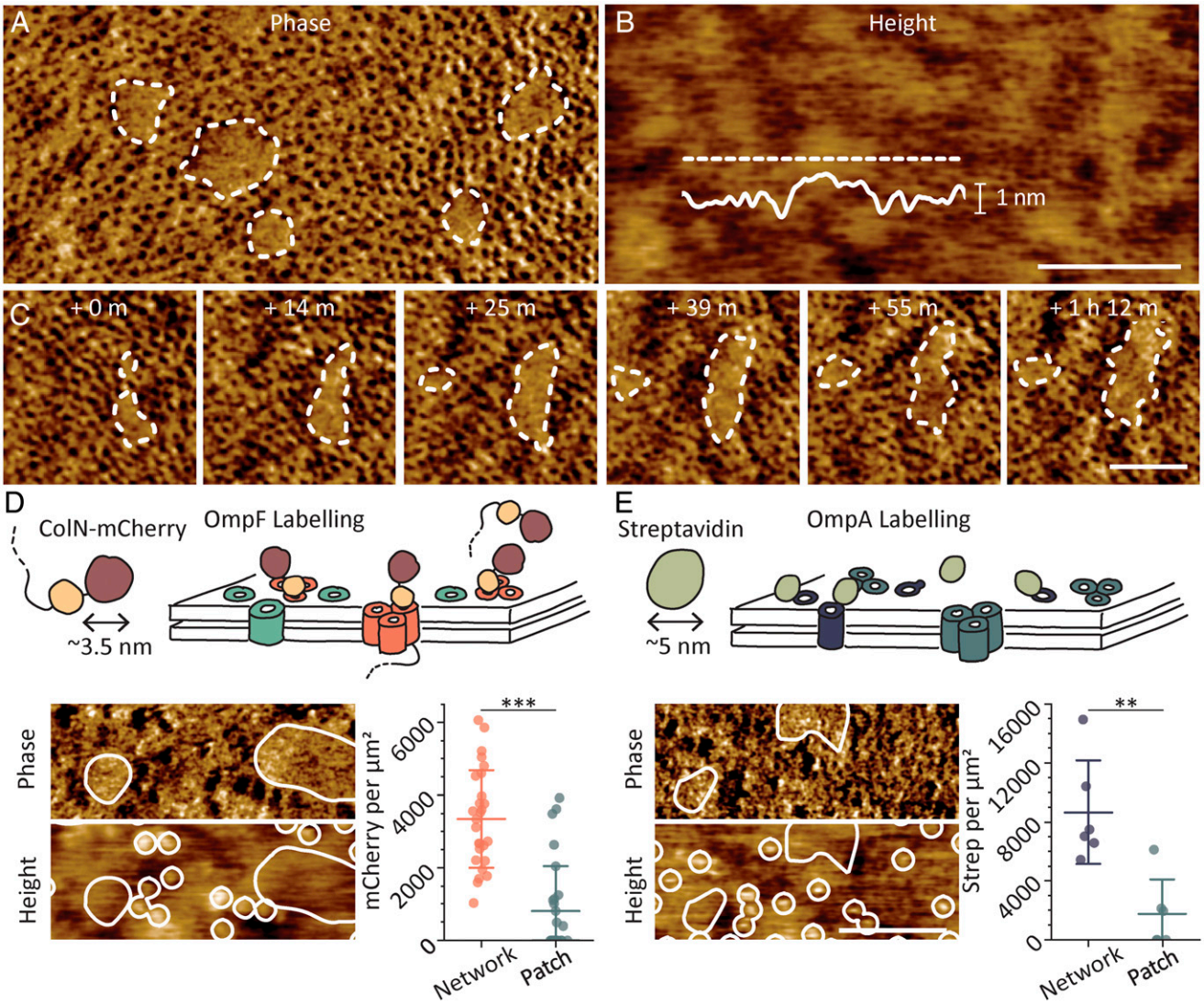

Fig. 2. Within the trimeric porin network, distinct pore-free patches that behave as liquid phases can be seen. (*A*) AFM phase image with patches highlighted by dashed lines. (*B*) Height image of the same area, showing that the patches protrude by about 1 nm. These regions are also extremely smooth, with height variations of less than 0.5 nm. (*C*) At timescales consistent with cell division, under these experimental conditions, patches merge, grow, and split apart. (*D*) Schematic of OmpF labeling by colicin $N^{1\text{-}185}$mCherry. Phase and height images of the same area are used to independently localize patches and labels, respectively. Quantification of the labels per area shows that OmpF colocalizes with the pore network. (*E*) OmpA is labeled by expressing ompA with a streptavidin binding peptide in an outer loop and adding streptavidin. Quantification of the labels per area shows that OmpA also colocalizes with pore networks. Each data point corresponds to a single image, in which images were recorded from three independent experiments with at least one cell per experiment. [Scale bars: (*B* and *E*) 100 nm and (*C*) 50 nm.] Color (phase/height) scales are (*A*) 1.5 deg, (*B*) 5 nm, (*C*) 1.5 deg, (*D*) 1.5 deg and 5 nm, and (*E*) 0.3 deg and 5 nm. ** = $P < 10^{-2}$ and *** = $P < 10^{-4}$ from a paired two-way Student's *t* test.

lateral positions at the bacterial surface (Fig. 2*C* and *SI Appendix*, Fig. S3 *C* and *D*).

The lack of pores in smooth OM patches suggests that they have a low protein content. To verify this, we specifically labeled trimeric OmpF and monomeric OmpA, as they are two of the most abundant OMPs in *E. coli*, each present at ~100,000 copies per cell (2, 27, 28). OmpF trimers were labeled by colicin $N^{1\text{-}185}$mCherry, which binds OmpF with high affinity (29). The diameter of the mCherry is ~3.5 nm (30): this is large enough to prevent entry into the porin and to thus block the translocation of the fused colicin through the OmpF, leaving the colicin $N^{1\text{-}185}$mCherry fusion in a partially translocated, tightly bound state. Importantly, it is also large enough to make it readily detectable via protrusions in the AFM height images. This allows the localization of mCherry molecules to single-nanometer resolution by AFM, without relying on fluorescence microscopy (Fig. 2*D*). These labels are poorly resolved in the AFM phase images of the same area, but in phase images, the patches are more easily distinguished and marked. This allowed the independent, unbiased detection of labels and patches. mCherry labels were found to localize only to the pore networks.

For OmpA, we used a similar AFM-based localization of a globular protein in the height images: *E. coli* MG1655 expressing *ompA* with a streptavidin-binding peptide in an outer loop (31) were labeled with streptavidin (Fig. 2*E*). The OmpA labels also colocalized with the pore networks but not with patches (Fig. 2*E*). Both for OmpF and OmpA labels, the colocalization with patches was at or below the noise floor due to false positives (*SI Appendix*, Fig. S4), suggesting that patches are largely or totally devoid of protein. This conclusion is further supported by the observation of smoother, presumably protein-free

patches against a rougher background in cells without OmpF and OmpC, with the roughness of the background assumed to be due to other OMPs (*SI Appendix*, Fig. S5). Taken together, our data demonstrates that distinct nanoscale, protein-poor domains are phase-separated from densely packed proteinaceous areas in the OM and gradually change during growth.

Since OMPs have been shown to readily interact with LPS by the structural resolution of LPS–OMP complexes (32, 33), it is likely that LPS is found throughout the membrane, including the pore network. However, because the smooth patches contained no detectable protein in our AFM studies, we hypothesized that they are instead enriched in or dominated by excess LPS. Therefore, larger expression levels of LPS were expected to lead to a larger part of the bacterial surface being covered by patches. To test this, the levels of LPS were modulated by altering the efficiency of LpxC (34) involved in the synthesis of lipid A in LPS (Fig. 3*A*). Increasing LPS production led to a significantly increased fraction of the bacterial surface being covered by smooth patches (Fig. 3*B* and *SI Appendix*, Fig. S6*A*), whereas the overall morphology of the patches and packing of the pore network remained the same (Fig. 3 *C–E* and *SI Appendix*, Figs. S6*B* and S7 *A* and *B*). The decrease in patch area with low LPS levels also coincided with an increase in pore density (*SI Appendix*, Fig. S7*C*) and slight decrease in mean patch size (Fig. 3*C*). The fact that the patch area is dependent on LPS abundance provides evidence that these patches are phase-separated, LPS-enriched domains.

If patches are indeed LPS-enriched phases, their phase separation from the proteinaceous network should be increased by promoting LPS–LPS interactions (compared with LPS–protein interactions). MG1655 have no O-antigen, so LPS are primarily bound together by Mg^{2+}, which strongly bridges the negatively charged LPS core (2). By reintroducing *wbbL*, the O-antigen is restored and the long polysaccharide chains enhance LPS–LPS interactions (35, 36). We predicted this would lead to a significant increase in typical patch size (area per patch), and this was indeed the case, with typical patch sizes notably exceeding those for wild type (WT) (Fig. 3*C*, MG1655 versus +*wbbL,* and *SI Appendix*, Fig. S6*A*).

Since the size of patches is dependent on LPS content and interaction strength, we conclude that they are indeed LPS-enriched. Furthermore, reported diffusion of LPS is slow (37, 38), which is consistent with gradual changes observed for the LPS-enriched patches (*SI Appendix*, Fig. S3 *C* and *D*).

Externalized Phospholipids Break the Porin Network to Form New Domains. Finally, the observation of LPS patches and protein-rich networks raises the question of how these arrangements are affected by phospholipids in the outer leaflet, which represent a disruption of the lipid asymmetry and lead to increased sensitivity toward detergents and the antibiotic bacitracin (39) (*SI Appendix*, Fig. S8*A*). Phospholipids are usually restricted to the inner leaflet by the Mla pathway and the phospholipase PldA: the combined deletion of *pldA* and disruption of the Mla pathway results in a ~25-fold enhancement of phospholipids in the outer leaflet compared with WT (11). This double deletion severely disrupts the OM permeability barrier, rendering the mutant strain sensitive to moderate concentrations of SDS-EDTA, as opposed to single *pldA* or *mlaA* deletions, which are as resistant as WT under those conditions (11) (*SI Appendix*, Fig. S8*A*).

Consistent with this physiological behavior, the morphology of the single Δ*mlaA* or Δ*pldA* mutants did not differ significantly from WT in our AFM assays, whereas Δ*mlaA* Δ*pldA* double mutant cells showed substantial changes in their OM architecture (Fig. 4 *A* and *B*). The Δ*mlaA* Δ*pldA* OMs showed abundant, high (~2 nm), pore-free protrusions, here referred to as phospholipid-enriched patches (Fig. 4). The phospholipid-

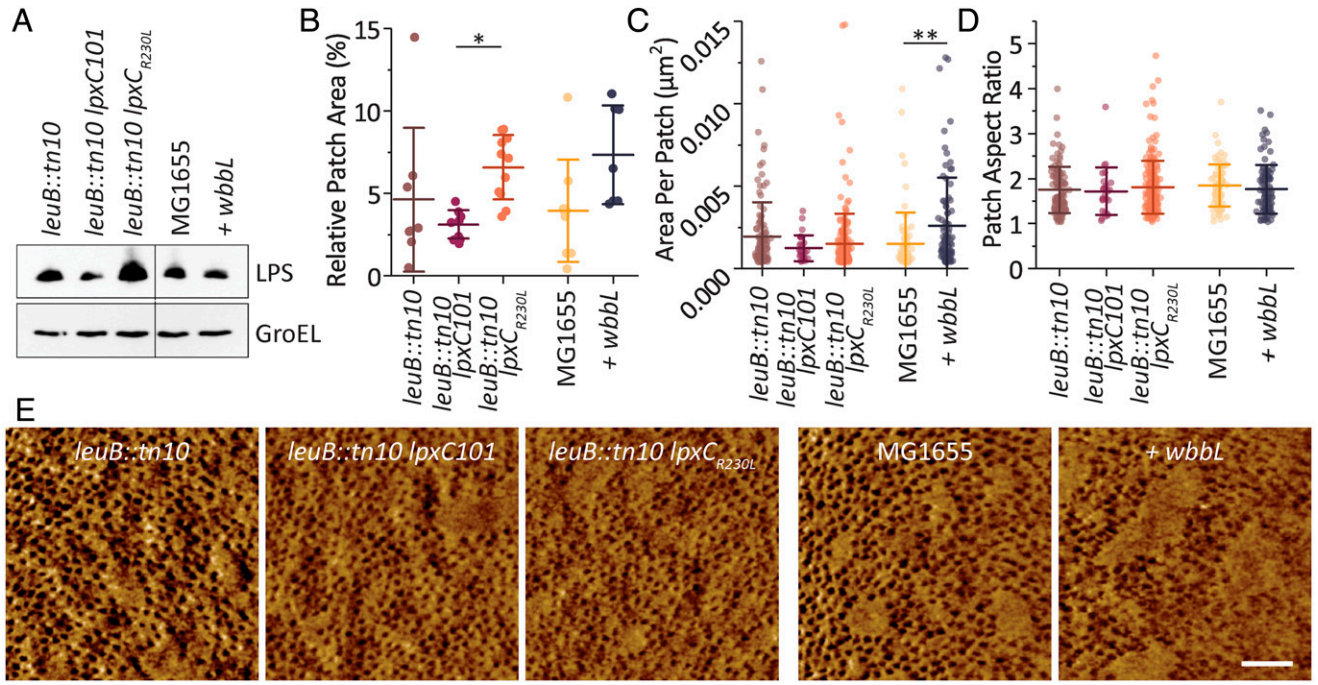

Fig. 3. Patches are LPS-enriched domains. (*A*) Western blot showing changes in LPS levels. (*B*) For low LPS levels (*lpxC101*), the cell area covered by patches is significantly smaller than for high LPS levels (*lpxC$_{R230L}$*). Reintroduction of O-antigen, and hence longer LPS (+*wbbL*), results in this area being almost twice that measured for WT (MG1655). Data were recorded in at least three independent experiments per condition; each data point represents one cell. (*C*) Longer LPS chains result in larger patches, and measurements for lower LPS expression suggest smaller patches. (*D*) Patch morphology (here quantified by the aspect ratio) does not noticeably vary with LPS expression. Each data point represents an individual patch from cells used in *B*. (*E*) Typical phase images used to quantify *B–D*. (Scale bar: 50 nm.) Color (phase/height) scale is 1.5 deg. * = $P < 0.05$ and ** = $P < 10^{-2}$.

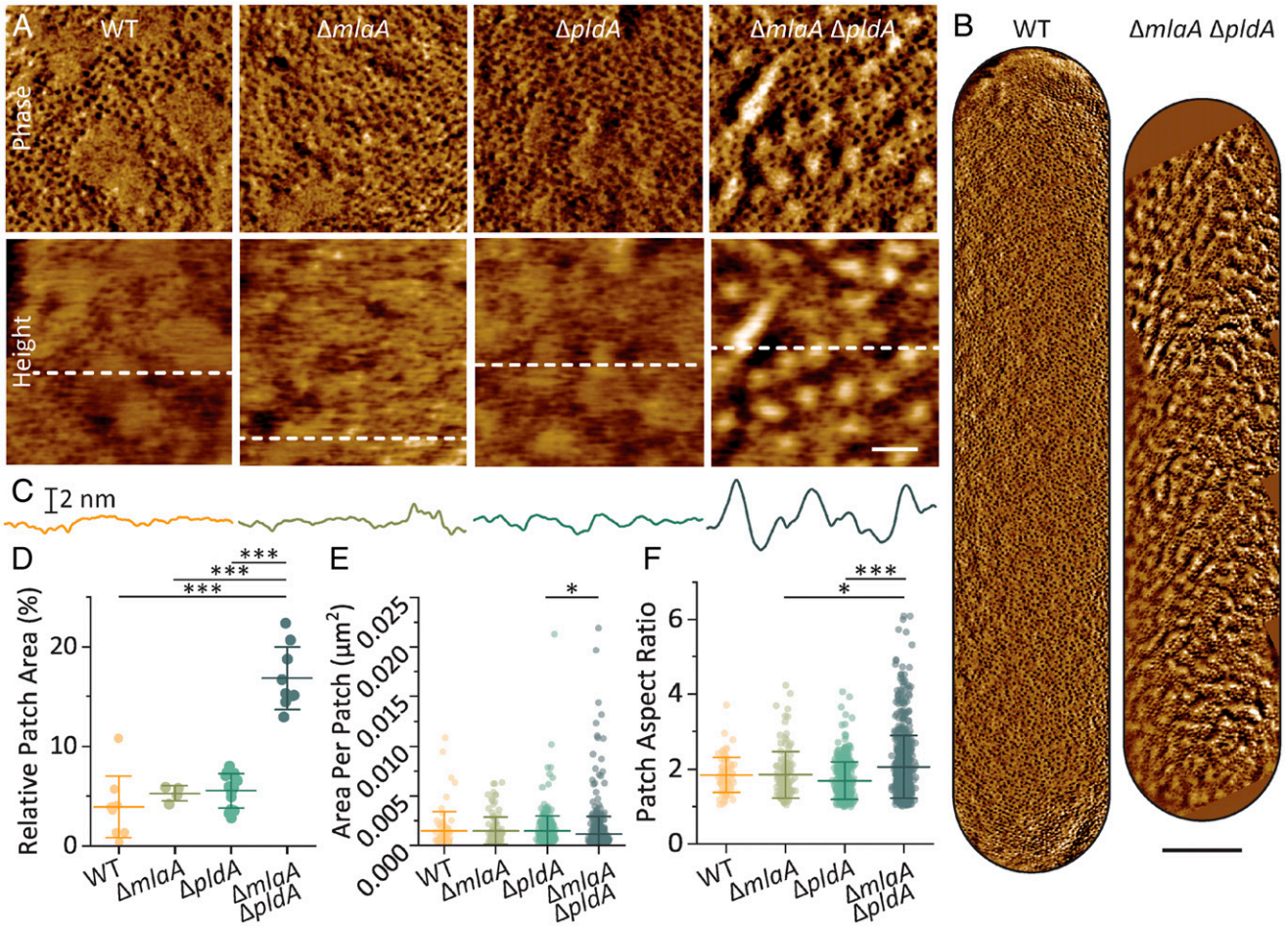

Fig. 4. Outer-leaflet phospholipids lead to the formation of new domains. (*A*) AFM phase and height images of cells with mutations that disrupt lipid asymmetry in the OM. (*B*) Whole-cell phase images of an MG1655 and a Δ*pldA* Δ*mlaA* cell showing the extent of membrane reorganization with abundant phospholipids. (*C*) Height profiles of dashed lines in the AFM images in *A*. (*D*) For Δ*pldA* Δ*mlaA* cells, a significantly larger fraction of the bacterial surface is covered by pore-free patches of either type, compared with WT and single mutants. Data were recorded in at least three independent experiments per condition; each data point represents one cell. (*E*) The mean area of each individual patch varies. Δ*pldA* Δ*mlaA* cells also have a greater spread of patch sizes. Each data point represents an individual patch from cells used in *D*. (*F*) The mean aspect ratios of Δ*pldA* Δ*mlaA* cells is higher than single mutants; an example of an elongated patch can be seen in *A*. [Scale bars: (*A*) 50 nm and (*B*) 200 nm.] Color (phase/height) scales are (*A*) 0.75 deg and 5, 4, 5 and 5 nm. * = $P < 0.05$ and *** = $P < 10^{-4}$.

enriched patches are distinct from LPS-enriched patches by this greater protrusion (height) and by their shape (Fig. 4*A*). Δ*mlaA* Δ*pldA* patches were found to be smaller, reflected by a lower mean area per patch (Fig. 4*E*), and any large Δ*mlaA* Δ*pldA* patches were elongated, shown by a higher patch aspect ratio (Fig. 4*F*). Additional evidence that phospholipids form new patches is seen, as LPS-enriched patches were observed alongside the abundant phospholipid-enriched patches on Δ*mlaA* Δ*pldA* cells (*SI Appendix*, Fig. S9).

Discussion

The lateral organization of OMPs and lipids provides important context for understanding their insertion into the OM (40) and, more generally, the architectural features that underpin OM function. For some OMPs, fluorescence microscopy has shown how promiscuous protein–protein interactions can lead to nonhomogenous patterning across the cell into OMP islands (4, 7–9, 41). In contrast, our results reveal an entirely different type of supramolecular organization in which an OMP network spans the entire bacterial surface and is only interrupted by nanoscale domains that are depleted of common OMPs and enriched in LPS.

Here, observed on live and metabolically active bacteria, the dense packing of OMPs is consistent with older electron microscopy data on freeze-fractured bacteria, which show the OM covered in proteins (23–26, 42). In addition, it is consistent with previous AFM results on small OM areas (12, 43–45) and on isolated OMs (46), which show similar arrangements of densely packed proteins at a local scale. Seen in the light of these previous results, our data provide further evidence that copies of abundant proteins (OmpF, OmpC, and OmpA) do not form isolated islands but fill the membrane with an imperfect protein lattice from pole to pole (Fig. 1). Notably, this does not preclude the existence—within the network—of islands of OMPs that, for example, have been synthesized or inserted at similar time points (4).

Although consistent with previous AFM analyses (44) and with single-molecule fluorescence microscopy of labeled OmpF (4, 27, 47), a puzzling aspect of this protein network is the near-static appearance of its constituents, since it raises the question of how the OM accommodates growth (4, 8, 27, 47, 48). Based on the results reported here, we speculate that LPS-enriched, OMP-depleted regions may facilitate insertion of new membrane components.

In addition to phase-separated LPS patches, different domains appear when phospholipids are present in the outer leaflet (Fig. 4), as here resulting from the combined deletion of *pldA* and disruption of the Mla pathway (11). These presumably phospholipid-enriched domains appear in the OMP network separate from the LPS domains. Their appearance is found to directly correlate with bacterial sensitivity to harsh environments, demonstrating a link between OM phase separation and functional behavior of gram-negative bacteria and explaining this enhanced sensitivity as due to local defects in the LPS–OMP dominated outer leaflet of the OM. The distinction between LPS-enriched patches and phospholipid-enriched patches is consistent with earlier evidence that LPS and phospholipids do not mix in the OM (49). It may also rationalize the association of MlaA with OmpC and OmpF in the OM (50), as this association could direct MlaA to the porin network, where the externalized phospholipids emerge (i.e., not in the LPS patches), to sense local OM disruption and activate retrograde transport of phospholipids to the inner membrane (11).

Taken together, these results represent the highest-resolution microscopy data of live cells reported to date and define the supramolecular architecture of the *E. coli* OM. Importantly, they provide a framework within which to understand associations between different OMPs, LPS, and phospholipids in the OM. Finally, this framework also provides a perspective to assess how bacterial sensitivity to immune effectors and antimicrobials may depend on local as well as global properties of the OM.

Materials and Methods

Bacterial Strains and Growth Conditions. All strains are shown in *SI Appendix*, Table S1. Unless otherwise stated, strains were constructed by generalized P1 transduction or transformation in *E. coli* strain MG1655 (51). Null alleles were obtained from the Keio collection (52), and FRT-flanked kanamycin resistance cassette was removed using the Flp recombinase system, as previously described (53). O-antigen was restored by introducing a WT copy of the *wbbL* gene at the native chromosomal locus. Production of O-antigen was assayed as gain of resistance against P1 phage (54). For AFM, bacteria were grown overnight in lysogeny broth (LB) at 37 °C, diluted 100× into fresh LB, and incubated for 2.5 more hours for exponentially growing cells. Where appropriate, LB was supplemented with 100 μg/mL ampicillin, 50 μg/mL kanamycin, 10 μg/mL tetracycline, 0.5% arabinose, 0.5% glucose, and 0.1% fucose.

Plasmid Construction. The plasmids used in this study are listed in *SI Appendix*, Table S2. To construct pBAD18::*ompR*, PCR was used to amplify the plasmid using oligonucleotides IMB89:pBAD18_openF (gaattcgagctcggtacc) and IMB90:pBAD18_openR (gctagcccaaaaaaacgg) and the *ompR* open reading frame using oligonucleotides IMB93:ompR_pBAD18F (acccgtttttttgggctagct cacacaggaaagggtggcatgcaagagaactac) and IMB94:ompR_pBAD18R (cgggtacc gagctcgaattctcatgctttagagccgtc). Products were purified using the QIAquick PCR purification kit (Qiagen) and assembled using Gibson Assembly (New England Biolabs).

Immunoblot Analysis. OD_{600} 1.0 exponentially growing cells were collected and lysed in 50 μL 2× Laemelli sample buffer (Bio-Rad) supplemented with β-mercaptoethanol (Sigma-Aldrich) by boiling for 10 min. A total of 8 μL sample was loaded and electrophoresed on a 10% SDS-PAGE gel. Proteins and LPS were transferred onto a nitrocellulose membrane using the Trans-Blot Turbo Transfer System (Bio-Rad). Membranes were blocked for 1 h in 5% milk at 4 °C, followed by incubation with primary antibody probing for αOmpF/C (1:10,000), αLPS (1:5,000; Hycult Biotech), or αGroEL (1:50,000; Sigma-Aldrich) overnight at 4 °C. Goat anti-rabbit IgG horseradish peroxidase (1:10,000; Sigma-Aldrich) or goat anti-mouse horseradish peroxidase (1:10,000; Bio-Rad) secondary antibodies were incubated for 1 h at room temperature.

OmpF Photoactivated Localization Microscopy Single Particle Tracking. Photoactivated localization microscopy single-particle tracking (PALM-SPT) was conducted on an Oxford Nanoimaging Ltd. Nanoimager S with a 100×, 1.49 numerical aperture objective. Overnight culture of MG1655 grown in M9 glucose (M9 minimal media + 0.05% [wt/vol] casamino acids, 0.4% D-glucose, 2 mM $MgSO_4$, and 0.1 mM $CaCl_2$) was transferred to 4 mL fresh M9 glucose and grown to an OD_{600} of 0.6 to 0.9. A volume of cells equivalent to 500 μL OD_{600} 0.6 culture was pelleted and resuspended in 200 μL fresh M9 glucose supplemented with 200 nM colicin $N^{1\text{-}185}$PAmCherry [expressed and purified in the same manner as colicin $N^{1\text{-}185}$mCherry (29)], and labeling of OmpF was allowed to proceed at room temperature for 10 min on a rotary shaker. Labeled cells were either fixed or prepared live for microscopy. Fixation was conducted by resuspension of a labeled cell pellet in 1 mL 4% formaldehyde for 30 min at 4 °C. Prior to loading cells onto slides, excess label was removed by four rounds of pelleting and resuspension (in phosphate-buffered saline [PBS] for fixed cells and M9 glucose for live cells). A total of 4 μL cells was loaded onto 1% agarose PBS pads and imaged. Room temperature PALM-SPT was conducted, and the data were analyzed as described in ref. 55.

Coverslip Preparation for AFM. The 13-mm glass coverslips (VWR) were sonicated in a 1 to 2% SDS solution in a Fisherbrand bath sonicator (Fisher Scientific) at 37 kHz and 100% power for 10 min. They were then rinsed in milliQ water (mQ), then ethanol, dried with nitrogen, and plasma cleaned in air at 70% power for 2 min. The whole procedure was then repeated. To ensure bacteria adhered to coverslips, they were soaked in a 50:1 solution of Acetone:Vectabond (Vector Laboratories) for 5 min, rinsed in mQ, and dried with nitrogen. Vectabond-coated coverslips were glued to clean glass slides using biocompatible glue (Reprorubber thin pour, Flexbar) and were not stored (12).

Preparation of Cells for AFM. For all AFM, except where specified otherwise, bacteria were prepared as follows. Freshly grown bacteria were washed three times by spinning for 2 min at 5,000 rpm and resuspending in minimal media (MM; 1× M9 salts (Thermo Fisher Scientific), 2 mM $MgSO_4$, 0.1 mM $CaCl_2$, and 0.36% glucose). A total of 100 μL washed cells was then resuspended in 20 mM Hepes and immediately applied to a Vectabond-coated coverslip for 5 min to adhere. For mechanical measurements, bacteria were resuspended in MM and applied to the coverslip for 30 min. The slide was then washed three times with 1 mL MM to remove unadhered bacteria and exchange buffers. With ∼100 μL volume on the coverslip, ∼5 μM SYTOX Green nucleic acid stain (Sigma-Aldrich) was added and incubated at room temperature for at least 5 min.

For streptavidin labeling, MG1655 pGV28 OmpA-SA1 cells (described in ref. 31) were induced with 2.2 mg/mL IPTG for 1 h during the 2.5-h growth. They were then washed three times in PBS, and 100 μL was applied to a Vectabond-coated coverslip for 30 min. The coverslip was washed three times with PBS, and SYTOX was added. When using streptavidin, 10 μg/mL was added and incubated on the slide for 30 min. SYTOX was then reapplied.

For colicin $N^{1\text{-}185}$mCherry labeling, exponential cells were washed three times by spinning for 1 min at 7,000 × *g* and resuspending in MM 0.4% (1× M9 salts, 2 mM $MgSO_4$, 0.1 mM $CaCl_2$, and 0.4% glucose). Cells were resuspended at OD_{600} 0.5. A total of 250 μL bacteria was then spun, resuspended in MM 0.4% with 0.1 μM Colicin $N^{1\text{-}185}$mCherry (unlabeled controls were resuspended in MM 0.4%), and incubated at room temperature on a rotary shaker for 5 min. Labeled cells were then washed with MM 0.4% three times by spinning and resuspending. Then, cells were resuspended in 100 μL 20 mM Hepes, applied to a Vectabond-coated coverslip for 5 min, and washed three times with 1 mL MM 0.4%.

AFM. All AFM was performed on a Nanowizard III AFM with UltraSpeed head (Bruker AXS) with an Andor Zyla 5.5 USB3 fluorescence camera on an Olympus IX 73 inverted optical microscope. AFM imaging was performed in dynamic (AC) mode with a FastScanD cantilever. The drive frequency was 90 to 140 kHz, depending on the cantilever resonance, with a setpoint of 5 to 15 nm (50 to 70% relative to free amplitude). The whole-cell image in Fig. 1 was acquired at 2 Hz, 2.5 μm^2, and 512 pixels. All other AC mode images are 500 nm and 512 pixels square, recorded at 2 to 8 Hz line frequency.

Mechanical measurements were performed in QI mode with a FastScanD (Bruker AXS) cantilever (0.25 N/m nominal spring constant and 110 kHz resonant frequency). For mechanical measurements, deflection sensitivity was calibrated by indenting cantilevers on glass up to a peak force of 0.2 nN with a 1-μm z-length; next, the cantilever stiffness was calibrated by measuring the thermal noise of the cantilever. The 500-nm scans were then taken on the surface of bacteria with 128 × 128 pixels, 0.1 nN set point, 90-nm z-length, and 30 $\mu m \cdot s^{-1}$ z-speed.

AFM Force Curve and Image Processing. QI mode images were analyzed in the JPK data-processing software. The effective Young's modulus was calculated using the Hertz–Sneddon model assuming a paraboloid tip shape, a radius of 2 nm, and a Poisson ratio of 0.5. Final images were imported into Gwyddion 2.52 (gwyddion.net/) (56) and the color scale set.

Fig. 1*A* was not postprocessed, but the color scale was set in Gwyddion. Small images were first processed with a Python script using Pygwy [from Gwyddion (56)] and originally adapted from AFM-SPM/TopoStats (57). The

script took Height and Phase channels of each image, applied a first-order polynomial fit to align rows, and exported the file as a text image. A custom FIJI-ImageJ (58) macro imported the text image, applied a high-pass filter (1 to 50 pixels, with 0.97 nm per pixel) to remove curvature of the cell, and a one-pixel Gaussian smoothing to reduce noise. Gwyddion was used for image representation and height profiles. Further analysis was performed as described in *Localization of Labels* and *Pore and Patch Analysis*.

Localization of Labels. Masks of patch regions were marked manually in FIJI-ImageJ using the phase channel because labels were poorly visible in the phase, meaning potential bias would be reduced. Labels were found by applying a high-pass filter (1 to 20 pixels, with 0.97 nm per pixel) and a two-pixel Gaussian blur to the height channel, then finding maxima with a prominence of 0.5 nm using a peak-search algorithm (the Find Maxima function in FIJI-ImageJ). The number of labels per square micrometer in patch and network areas were calculated in MATLAB (Mathworks).

Pore and Patch Analysis. For high-resolution whole-cell images required for pore and patch finding, 500-nm scans were performed across the bacterial surface. The approximate location of each scan is recorded in the jpk file and was accessed in the JPK data-processing software. Individual phase scans were then accurately overlaid in FIJI-ImageJ by comparing surface features in each image. Once overlays covering the accessible cell surface were complete, a mask of patches was generated by manually marking patch edges in FIJI-ImageJ. Any patch less than about 400 nm^2 was ignored, as their identification was often ambiguous. To calculate the relative patch area, the area of bacterial surface imaged was outlined manually and the percentage imaged area taken up by patches was calculated in MATLAB (Mathworks). The FIJI-ImageJ shape descriptors function was used to find patch aspect ratios and individual patch areas.

For pore locations, the Find Maxima function in FIJI-ImageJ was first used to find potential pores. Any points that fell outside the imaged area were ignored, and the remaining points were exported as coordinates. The Enhance Local Contrast function was then used to normalize contrast across the surface, since contrast was usually higher at the edges of cells. Uncorrected, this led to central pores being missed. The corrected image was exported as an 8-bit with potential pore coordinates. Actual pores were then found using a machine-learning model described in *Pore Finding*. Nearest-neighbor and angular distributions were determined using custom MATLAB scripts (available at https://github.com/hoogenboom-lab/image-analysis). For angular distributions, neighbors less than 15 nm were found for each pore, and the angle between each of these neighbors, with respect to the center pore, was found.

For diffusion analysis, time-lapse images were recorded at 91 s per frame for 20 min. Crops were taken of different locations within the image, and pores were identified and tracked manually from frame to frame. For each pair of pores at positions $\mathbf{r}_i = (x_i, y_i)$ and $\mathbf{r}_j = (x_j, y_j)$, the autocorrelation function was calculated $\langle \mathbf{r}_i(t) \cdot \mathbf{r}_j(t+\tau) \rangle \approx -2D\tau$, where D is the diffusion coefficient and τ is the delay time (59). The pore diffusion coefficient was then calculated from the slope of the autocorrelation function.

Pore Finding. The labeling of pores in a cell image was performed using a machine-learning model for object detection. A two-state image classifier was first developed to distinguish between images of pores and images of cell membrane in which pores were not present. This model used a gradient-boosted decisions trees method (60) with 50 weak learner models and used mean cross entropy as its loss function. Details of the method and a learning curve can be found in *SI Appendix*, Table S3 and Fig. S10. The method was chosen based on its performance after multiple methods were tested by the Wolfram Mathematica Classify function (61).

The model was trained using a diverse set of cell images in which pores had been labeled manually. Training data for the "pore" class was generated by taking a 9×9 pixel region around the manually labeled pore center, while data from the "not pore" class was generated by sampling the complement of the "pore" regions and the original image. This produced a total dataset of 36,392 pore images and 1,157,455 nonpore images; of these, around 80% of each set were used for training and around 20% (235,267 images total) were held back for testing. To account for the imbalance between the minority and majority class, the remaining pore class was oversampled to 10% of the majority class size, producing a final training set of 116,456 pore images and 925,964 nonpore images (or 1,042,420 images in total). A mosaic of a small sample of each class of the training set is provided in *SI Appendix*, Fig. S11*A*.

With this method, the classifier achieved an accuracy of 97.7% and an F_1 score of 0.696. The confusion matrix from which these values are derived is given in *SI Appendix*, Fig. S11*B*. It is notable that the model's high accuracy may be skewed by the imbalance in the class sizes and so cannot be considered a measure of performance when taken in isolation. The difficulty associated with the manual labeling of pores to be included in the training set may account for the low precision (the proportion of "pore" predictions that were correct). By visual inspection of marked cells, the model found 90% of the pores present in images with few false positives, which was sufficiently accurate to label pores in real data.

To find pores in the data, the classifier was used as part of a scrolling window object detection routine in which each 9×9 region around the pixels in a given region of a cell image were classified by the model. To reduce the region of the image to be sampled for classification, this was preceded by the step that identified the local brightness minima of the image in which pores were most likely to appear, and only the 11×11 pixel regions around these minima were checked by the scrolling window. This resulted in a set of labeled pixels for each image, which were considered part of a pore (*SI Appendix*, Fig. S11*C*). These regions had a Gaussian blur of radius-0.5 pixels applied in order to combine the labels of elongated or conjoined pores. The centroids of these regions were then found by applying image segmentation [via the Mathematica ComponentMeasurements function (62)], giving the final estimate of the center point of the pores in the image. Using this method allowed for images to be labeled far more quickly than they would be manually and with a greater accuracy than traditional image analysis approaches.

Graphing and Statistics. All graphing and statistics were performed in OriginPro (OriginLab). Statistical tests are from a one-way ANOVA with Tukey's *t* test, and mean lines and SDs are shown in plots unless otherwise stated.

Data Availability. Data supporting this study are available online in the University College London Research Data Repository under DOI 10.5522/04/16547644.

ACKNOWLEDGMENTS. We acknowledge Dr. Richard Thorogate for technical support, Tanneke den Blaauwen for providing the pGV28 OmpA-SA1 plasmid, and Guillermo Herrera-Sanchez for assistance with computational analysis. Research reported in this publication was funded by the United Kingdom Research and Innovation Biotechnology and Biological Sciences Research Council (BB/R000042/1 to B.W.H.), Engineering and Physical Sciences Research Council (EP/N509577/1 to G.B. and B.W.H.; EP/K031953/1 for equipment via the Interdisciplinary Research Centre in Early-Warning Sensing Systems for Infectious Diseases), funding from the UK Department for Business, Energy and Industrial Strategy (to G.B. and M.G.R.) and Medical Research Council (MR/R000328/1 to B.W.H.), and by the National Institute of General Medical Sciences of the NIH under Award Nos. F32GM139232 (to I.V.M.) and R35-GM118024 (to T.J.S.). The content is solely the responsibility of the authors and does not necessarily represent the official views of the NIH (or other funders). C.K. acknowledges funding for this work from the European Research Council (Advanced Grant 742555; OMPorg). P.G.I. acknowledges studentship funding from the UK Medical Research Council.

1. E. R. Rojas *et al.*, The outer membrane is an essential load-bearing element in Gram-negative bacteria. *Nature* **559**, 617–621 (2018).
2. T. J. Silhavy, D. Kahne, S. Walker, The bacterial cell envelope. *Cold Spring Harb. Perspect. Biol.* **2**, a000414 (2010).
3. R. Koebnik, K. P. Locher, P. Van Gelder, Structure and function of bacterial outer membrane proteins: Barrels in a nutshell. *Mol. Microbiol.* **37**, 239–253 (2000).
4. P. Rassam *et al.*, Supramolecular assemblies underpin turnover of outer membrane proteins in bacteria. *Nature* **523**, 333–336 (2015).
5. A. S. Ghosh, K. D. Young, Helical disposition of proteins and lipopolysaccharide in the outer membrane of *Escherichia coli*. *J. Bacteriol.* **187**, 1913–1922 (2005).
6. N. Paracini, L. A. Clifton, M. W. A. Skoda, J. H. Lakey, Liquid crystalline bacterial outer membranes are critical for antibiotic susceptibility. *Proc. Natl. Acad. Sci. U.S.A.* **115**, E7587–E7594 (2018).
7. G. Mamou *et al.*, Spatiotemporal organization of BamA governs the pattern of outer membrane protein distribution in growing *Escherichia coli* cells. bioRxiv [Preprint] (2021). https://doi.org/10.1101/2021.01.27.428258 (Accessed 6 May 2021).
8. S. D. Gunasinghe *et al.*, The WD40 protein BamB mediates coupling of BAM complexes into assembly precincts in the bacterial outer membrane. *Cell Rep.* **23**, 2782–2794 (2018).
9. C. Kleanthous, P. Rassam, C. G. Baumann, Protein-protein interactions and the spatiotemporal dynamics of bacterial outer membrane proteins. *Curr. Opin. Struct. Biol.* **35**, 109–115 (2015).
10. R. N. Reusch, Insights into the structure and assembly of *Escherichia coli* outer membrane protein A. *FEBS J.* **279**, 894–909 (2012).
11. J. C. Malinverni, T. J. Silhavy, An ABC transport system that maintains lipid asymmetry in the gram-negative outer membrane. *Proc. Natl. Acad. Sci. U.S.A.* **106**, 8009–8014 (2009).

12. G. Benn, A. L. B. Pyne, M. G. Ryadnov, B. W. Hoogenboom, Imaging live bacteria at the nanoscale: Comparison of immobilisation strategies. *Analyst (Lond.)* **144**, 6944–6952 (2019).
13. A. Viljoen, S. J. Foster, G. E. Fantner, J. K. Hobbs, Y. F. Dufrêne, Scratching the surface: Bacterial cell envelopes at the nanoscale. *MBio* **11**, e03020-19 (2020).
14. R. García, R. Pérez, Dynamic atomic force microscopy methods. *Surf. Sci. Rep.* **47**, 197–301 (2002).
15. D. L. Dorset, A. Engel, M. Häner, A. Massalski, J. P. Rosenbusch, Two-dimensional crystal packing of matrix porin. A channel forming protein in *Escherichia coli* outer membranes. *J. Mol. Biol.* **165**, 701–710 (1983).
16. H. J. Sass *et al.*, Densely packed β-structure at the protein-lipid interface of porin is revealed by high-resolution cryo-electron microscopy. *J. Mol. Biol.* **209**, 171–175 (1989).
17. M. Simón, A. Mathes, A. Blanch, H. Engelhardt, Characterization of a porin from the outer membrane of *Vibrio anguillarum*. *J. Bacteriol.* **178**, 4182–4188 (1996).
18. F. A. Schabert, A. Engel, Reproducible acquisition of *Escherichia coli* porin surface topographs by atomic force microscopy. *Biophys. J.* **67**, 2394–2403 (1994).
19. F. A. Schabert, C. Henn, A. Engel, Native Escherichia coli OmpF porin surfaces probed by atomic force microscopy. *Science* **268**, 92–94 (1995).
20. J. P. Rosenbusch, Characterization of the major envelope protein from *Escherichia coli*. Regular arrangement on the peptidoglycan and unusual dodecyl sulfate binding. *J. Biol. Chem.* **249**, 8019–8029 (1974).
21. S. W. Cowan *et al.*, The structure of OmpF porin in a tetragonal crystal form. *Structure* **3**, 1041–1050 (1995).
22. R. K. Taylor, M. N. Hall, L. Enquist, T. J. Silhavy, Identification of OmpR: A positive regulatory protein controlling expression of the major outer membrane matrix porin proteins of *Escherichia coli* K-12. *J. Bacteriol.* **147**, 255–258 (1981).
23. M. E. Bayer, C. C. Remsen, Structure of *Escherichia coli* after freeze-etching. *J. Bacteriol.* **101**, 304–313 (1970).
24. M. E. Bayer, L. Leive, Effect of ethylenediaminetetraacetate upon the surface of *Escherichia coli*. *J. Bacteriol.* **130**, 1364–1381 (1977).
25. L. van Alphen, A. Verkleij, J. Leunissen-Bijvelt, B. Lugtenberg, Architecture of the outer membrane of *Escherichia coli*. III. Protein-lipopolysaccharide complexes in intramembraneous particles. *J. Bacteriol.* **134**, 1089–1098 (1978).
26. U. B. Sleytr, M. J. Thornley, A. M. Glauert, Location of the fracture faces within the cell envelope of *Acinetobacter* species strain MJT-F5-5. *J. Bacteriol.* **118**, 693–707 (1974).
27. P. Rassam *et al.*, Intermembrane crosstalk drives inner-membrane protein organization in *Escherichia coli*. *Nat. Commun.* **9**, 1082 (2018).
28. M. L. Ortiz-Suarez, F. Samsudin, T. J. Piggot, P. J. Bond, S. Khalid, Full-length OmpA: Structure, function, and membrane interactions predicted by molecular dynamics simulations. *Biophys. J.* **111**, 1692–1702 (2016).
29. K. B. Jansen *et al.*, Bifurcated binding of the OmpF receptor underpins import of the bacteriocin colicin N into *Escherichia coli*. *J. Biol. Chem.* **295**, 9147–9156 (2020).
30. X. Shu, N. C. Shaner, C. A. Yarbrough, R. Y. Tsien, S. J. Remington, Novel chromophores and buried charges control color in mFruits. *Biochemistry* **45**, 9639–9647 (2006).
31. G. S. Verhoeven, S. Alexeeva, M. Dogterom, T. den Blaauwen, Differential bacterial surface display of peptides by the transmembrane domain of OmpA. *PLoS One* **4**, e6739 (2009).
32. A. D. Ferguson, E. Hofmann, J. W. Coulton, K. Diederichs, W. Welte, Siderophore-mediated iron transport: Crystal structure of FhuA with bound lipopolysaccharide. *Science* **282**, 2215–2220 (1998).
33. W. Arunmanee *et al.*, Gram-negative trimeric porins have specific LPS binding sites that are essential for porin biogenesis. *Proc. Natl. Acad. Sci. U.S.A.* **113**, E5034–E5043 (2016).
34. R. L. Guest, D. Samé Guerra, M. Wissler, J. Grimm, T. J. Silhavy, YejM modulates activity of the YciM/FtsH protease complex to prevent lethal accumulation of lipopolysaccharide. *mBio* **11**, 1–13 (2020).
35. D. Jefferies, J. Shearer, S. Khalid, Role of O-antigen in response to mechanical stress of the *E. coli* outer membrane: Insights from coarse-grained MD simulations. *J. Phys. Chem. B* **123**, 3567–3575 (2019).
36. P. R. Reeves, M. M. Cunneen, "Chapter 18 - Biosynthesis of O-antigen chains and assembly" in *Microbial Glycobiology*, O. Holst, P. J. Brennan, M. von Itzstein, A. P. Moran, Eds. (Academic Press, 2010), pp. 319–335.
37. S. D. Gunasinghe, C. T. Webb, K. D. Elgass, I. D. Hay, T. Lithgow, Super-resolution imaging of protein secretion systems and the cell surface of Gram-negative bacteria. *Front. Cell. Infect. Microbiol.* **7**, 220 (2017).
38. M. Schindler, M. J. Osborn, D. E. Koppel, Lateral diffusion of lipopolysaccharide in the outer membrane of *Salmonella typhimurium*. *Nature* **285**, 261–263 (1980).
39. M. Vaara, Antibiotic-supersusceptible mutants of *Escherichia coli* and *Salmonella typhimurium*. *Antimicrob. Agents Chemother.* **37**, 2255–2260 (1993).
40. J. E. Horne, D. J. Brockwell, S. E. Radford, Role of the lipid bilayer in outer membrane protein folding in Gram-negative bacteria. *J. Biol. Chem.* **295**, 10340–10367 (2020).
41. T. S. Ursell, E. H. Trepagnier, K. C. Huang, J. A. Theriot, Analysis of surface protein expression reveals the growth pattern of the gram-negative outer membrane. *PLOS Comput. Biol.* **8**, e1002680 (2012).
42. B. Lugtenberg, L. Van Alphen, Molecular architecture and functioning of the outer membrane of *Escherichia coli* and other gram-negative bacteria. *Biochim. Biophys. Acta* **737**, 51–115 (1983).
43. Z. Oestreicher, A. Taoka, Y. Fukumori, A comparison of the surface nanostructure from two different types of gram-negative cells: *Escherichia coli* and *Rhodobacter sphaeroides*. *Micron* **72**, 8–14 (2015).
44. H. Yamashita *et al.*, Single-molecule imaging on living bacterial cell surface by high-speed AFM. *J. Mol. Biol.* **422**, 300–309 (2012).
45. D. A. Heesterbeek *et al.*, Bacterial killing by complement requires membrane attack complex formation via surface-bound C5 convertases. *EMBO J.* **38**, 99852 (2019).
46. S. Jarosławski, K. Duquesne, J. N. Sturgis, S. Scheuring, High-resolution architecture of the outer membrane of the Gram-negative bacteria *Roseobacter denitrificans*. *Mol. Microbiol.* **74**, 1211–1222 (2009).
47. M. Chavent *et al.*, How nanoscale protein interactions determine the mesoscale dynamic organisation of bacterial outer membrane proteins. *Nat. Commun.* **9**, 2846 (2018).
48. A. Paraschiv, S. Hegde, R. Ganti, T. Pilizota, A. Šarić, Dynamic clustering regulates activity of mechanosensitive membrane channels. *Phys. Rev. Lett.* **124**, 048102 (2020).
49. H. Nikaido, Y. Takeuchi, S. I. Ohnishi, T. Nakae, Outer membrane of *Salmonella typhimurium*. Electron spin resonance studies. *Biochim. Biophys. Acta* **465**, 152–164 (1977).
50. Z. S. Chong, W. F. Woo, S. S. Chng, Osmoporin OmpC forms a complex with MlaA to maintain outer membrane lipid asymmetry in *Escherichia coli*. *Mol. Microbiol.* **98**, 1133–1146 (2015).
51. T. Silhavy, M. Berman, L. Enquist, *Experiments with Gene Fusions* (Cold Spring Harb. Lab., Cold Spring Harbor, NY, 1984).
52. T. Baba *et al.*, Construction of *Escherichia coli* K-12 in-frame, single-gene knockout mutants: The Keio collection. *Mol. Syst. Biol.*, 10.1038/msb4100050 (2006).
53. P. P. Cherepanov, W. Wackernagel, Gene disruption in *Escherichia coli*: TcR and KmR cassettes with the option of Flp-catalyzed excision of the antibiotic-resistance determinant. *Gene* **158**, 9–14 (1995).
54. T. D. Ho, M. K. Waldor, Enterohemorrhagic *Escherichia coli* O157:H7 gal mutants are sensitive to bacteriophage P1 and defective in intestinal colonization. *Infect. Immun.* **75**, 1661–1666 (2007).
55. J. Szczepaniak *et al.*, The lipoprotein Pal stabilises the bacterial outer membrane during constriction by a mobilisation-and-capture mechanism. *Nat. Commun.* **11**, 1305 (2020).
56. D. Nečas, P. Klapetek, Gwyddion: An open-source software for SPM data analysis. *Cent. Eur. J. Phys.* **10**, 181–188 (2012).
57. J. G. Beton *et al.*, TopoStats–A program for automated tracing of biomolecules from AFM images. *Methods* **193**, 68–79 (2021).
58. J. Schindelin *et al.*, Fiji: An open-source platform for biological-image analysis. *Nat. Methods* **9**, 676–682 (2012).
59. B. Tränkle, D. Ruh, A. Rohrbach, Interaction dynamics of two diffusing particles: Contact times and influence of nearby surfaces. *Soft Matter* **12**, 2729–2736 (2016).
60. J. H. Friedman, Greedy function approximation: A gradient boosting machine. *Ann. Stat.* **29**, 1189–1232 (2001).
61. Wolfram Research, Classify, Wolfram Language function (2014). https://reference.wolfram.com/language/ref/Classify.html. Accessed 13 May 2021.
62. Wolfram Research, ComponentMeasurements, Wolfram Language function (2010). https://reference.wolfram.com/language/ref/ComponentMeasurements.html. Accessed 13 May 2021.